Icarus 235 (2014) 23–36

Contents lists available at ScienceDirect

Icarus

journal homepage: www.elsevier.com/locate/icarus

The production of small primary craters on Mars and the Moon

Jean-Pierre Williams [a,*], Asmin V. Pathare [b], Oded Aharonson [c]

[a] Dept. Earth, Planetary and Space Sciences, University of California, Los Angeles, CA 90095, USA
[b] Planetary Science Institute, Tucson, AZ 85719, USA
[c] Helen Kimmel Center for Planetary Science, Weizmann Institute of Science, Rehovot 76100, Israel

ARTICLE INFO

Article history:
Received 18 June 2013
Revised 20 February 2014
Accepted 8 March 2014
Available online 17 March 2014

Keywords:
Cratering
Mars
Mars, surface

ABSTRACT

We model the primary crater production of small ($D < 100$ m) primary craters on Mars and the Moon using the observed annual flux of terrestrial fireballs. From the size–frequency distribution (SFD) of meteor diameters, with appropriate velocity distributions for Mars and the Moon, we are able to reproduce martian and lunar crater-count chronometry systems (isochrons) in both slope and magnitude. We include an atmospheric model for Mars that accounts for the deceleration, ablation, and fragmentation of meteors. We find that the details of the atmosphere or the fragmentation of the meteors do not strongly influence our results. The downturn in the crater SFD from atmospheric filtering is predicted to occur at $D \sim 10$–20 cm, well below the downturn observed in the distribution of fresh craters detected by the Mars Global Surveyor (MGS) Mars Orbiter Camera (MOC) or the Mars Reconnaissance Orbiter (MRO) Context Camera (CTX). Crater counts are conducted on the ejecta blanket of Zunil crater and the interior of Pangboche crater on Mars and North Ray and Cone craters on the Moon. Our model isochrons produce a similar slope and age estimate for the formation of Zunil crater as the Hartmann production function (~1 Ma). We derive an age of 35.1 Ma for Pangboche when accounting for the higher elevation (>20 km higher than Zunil), a factor ~2 younger than estimated using the Hartmann production function which assumes 6 mbar surface pressure. We estimate ages of 52.3 Ma and 23.9 Ma for North Ray and Cone crater respectively, consistent with cosmic ray exposure ages from Apollo samples. Our results indicate that the average cratering rate has been constant on these bodies over these time periods. Since our Monte Carlo simulations demonstrate that the existing crater chronology systems can be applied to date young surfaces using small craters on the Moon and Mars, we conclude that the signal from secondary craters in the isochrons must be relatively small at these locations, as our Monte Carlo model only generates primary craters.

1. Introduction

The accumulation of craters on a planetary surface can be used to determine relative ages of areas of geologic interest. Assigning absolute ages is done with modeled impact crater isochrons, a technique that has been developed over several decades (e.g. Hartmann, 1966, 1999, 2005; Neukum and Wise, 1976; Neukum and Ivanov, 1994; Hartmann and Neukum, 2001). For crater ages on Mars, isochrons are derived from the size–frequency distribution (SFD) of craters observed on the lunar maria for which we have dated Apollo samples (Wilhelms, 1987), scaled to account for the ratio of meteoroids at the top of the martian atmosphere relative to the Moon's and the differences in gravity and average impact velocity of intersecting orbits. The resulting isochrons yield an expected crater SFD for a given age surface and provide a means of understanding the absolute timescale of major geological and geophysical processes.

The SFD is typically described as a power-law with slope n. Deviations from the power-law occur through various processes which, in general, preferentially alter the smaller diameter crater population, making small craters more challenging to use for age-dating surfaces. Because of the frequency at which small craters form however, they provide the ability to discriminate surface ages of geologically young regions and features at a higher spatial resolution where only small craters are available for dating. This level of resolution is required to establish the temporal relation of recent geologic activity on Mars such as gully and landslide formation, volcanic resurfacing, sedimentation, exhumation, dune activity, glaciation and other periglacial landforms, and the possible relation of such features to obliquity cycles of $\sim 10^7$ yr

* Corresponding author. Fax: +1 310 825 2279.
E-mail addresses: jpierre@mars.ucla.edu (J.-P. Williams), pathare@psi.edu (A.V. Pathare), Oded.Aharonson@weizmann.ac.il (O. Aharonson).

http://dx.doi.org/10.1016/j.icarus.2014.03.011
0019-1035/

timescale (e.g. Basilevsky et al., 2009; Burr et al., 2002; Hartmann and Berman, 2000; Kadish et al., 2008; Lanagan et al., 2001; Malin and Edgett, 2000a, 2000b, 2001; Mangold, 2003; Marquez et al., 2004; Quantin et al., 2007; Reiss et al., 2004; Shean et al., 2006; Schon et al., 2009).

The Mars Obiter Camera (MOC) aboard the Mars Global Surveyor (MGS), with ~1.5 m resolution/pixel (Malin et al., 1992), identified 19 fresh craters over a ~6.8 yr period (Malin et al., 2006). Data from the High Resolution Imaging Science Experiment (HiRISE) aboard the Mars Reconnaissance Orbiter (MRO) is currently providing image data with up to 25 cm pix^{-1} resolution (McEwen et al., 2007a), and has imaged and confirmed >200 small (<50 m diameter) fresh impact craters having formed within the last few decades following their discovery by the Context (CTX) camera (Malin et al., 2007) on the same spacecraft (Byrne et al., 2009; Daubar et al., 2010, 2011; Daubar and McEwen, 2009; Dundas and Byrne, 2010; Ivanov et al., 2008, 2009, 2010; Kennedy and Malin, 2009; McEwen et al., 2007b, 2007c). This offers an opportunity to study the production of small meter-scale craters on the surface of Mars in greater detail and refine isochron models for dating young surfaces on Mars.

In this paper, we model crater populations using a Monte Carlo simulation to explore the primary crater production function at small diameters and the potential influence of present-day atmospheric filtering. We explore ablation, deceleration, and fragmentation of projectiles as they traverse the martian atmosphere. With this approach, we generate impact-crater isochrons and compare our results with the 44 fresh craters reported by Daubar et al. (2013) that have been well constrained by CTX before- and after-images and the current impact-crater isochron models for Mars (Hartmann, 2005) and the Moon (Neukum et al., 2001).

2. Model

2.1. Meteoroids traversing the martian atmosphere

Crater populations are modeled assuming a power law distribution of projectiles at the top of the atmosphere and account for possible fragmentation and the dependence of mass and velocity on deceleration and ablation in the atmosphere. The size distribution of projectiles at the top of Mars' atmosphere is adapted from the power-law fit to satellite observations of the annual flux of near-Earth objects colliding with the Earth for objects with diameters <200 m (Brown et al., 2002): $\log(N) = a_o - b_o \log(E)$, where N is the cumulative number of bolides colliding with the Earth per year with energies of E and greater (in ktons), $a_o = 0.5677 \pm 0.015$, and $b_o = 0.90 \pm 0.03$.

The kinetic energy of an object entering the atmosphere is lost to deceleration and ablation. The decelerating force due to aerodynamic drag is (e.g., Baldwin and Sheaffer, 1971; Chyba et al., 1993; Melosh, 1989)

$$\frac{dv}{dt} = \frac{C_D \rho_a A v^2}{2m} + g(z)\sin\theta \quad (1)$$

where ρ_a is the local density of the atmosphere. The parameters A, v, and m, are the cross-sectional area, the velocity, and the mass of the object respectively, g is the local gravitational acceleration at altitude z, and θ is the angle of the trajectory measured from the local horizontal

$$\frac{d\theta}{dt} = \frac{g(z)\cos\theta}{v} \quad (2)$$

Eq. (2) assumes a flat surface geometry and precludes the possibility of projectiles skipping out of the atmosphere. The drag coefficient, C_D, is ~1 for a spherical body in the continuum flow regime (Podolak et al., 1988). Heating of the projectile's surface during entry is efficiently shed by ablation

$$\frac{dm}{dt} = \frac{C_H \rho_a A v^3}{2\zeta} \quad (3)$$

where C_H is the heat transfer coefficient and ζ is the heat of ablation (Bronshten, 1983). The coefficients in Eqs. (2) and (3) are related by the ablation coefficient, $\sigma = C_H/(2\zeta C_D)$.

To assess the conditions in which deceleration and ablation become substantial, we employ a heuristic model. Taking the gravity term to be negligible in Eq. (1) for the moment, and the approximation of an exponential density scale height for the atmosphere ($\rho_a = \rho_o \exp(-z/H)$, where z is the altitude, H is the scale height, and ρ_o is the atmospheric density at the surface), the final mass of the meteor, m_f, can be related to the initial velocity, v_i, and final velocity, v_f, by

$$m_f = m_i \exp\left[-\sigma\left(v_i^2 - v_f^2\right)\right] \quad (4)$$

where m_i is the initial mass of the object at entry (Ceplecha et al., 1998).

Combining the above equations and solving (e.g., Davis, 1993), the dependence of mass and velocity on deceleration and ablation can be seen (Fig. 1). Smaller, faster objects are more readily filtered out by the atmosphere. The condition for significant deceleration can be estimated to occur when the meteoroid mass is equivalent to the column of atmospheric mass it encounters, $m_i \sim \rho_o HA$. Similarly, we can estimate the condition for substantial ablation, which is more efficient at higher velocities as the ablative energy is proportional to the product of the drag force and the traversed

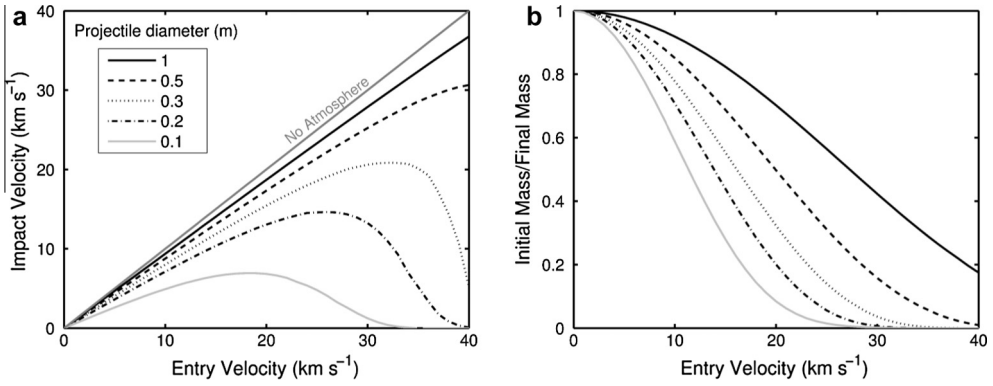

Fig. 1. (a) Initial velocity versus final velocity and (b) the ratio of initial and final projectile mass versus initial velocity for a range of projectile diameters (10 cm to 1 m), where objects have properties of Ordinary Chondrites (Table 1). Smaller, faster objects are more effectively decelerated and ablated.

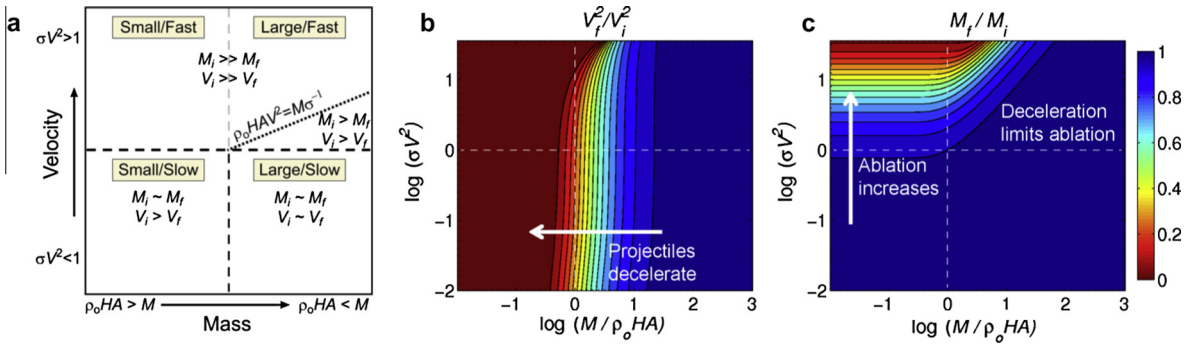

Fig. 2. (a) General classes of projectiles based on initial mass and velocity. *Large, slow projectiles*: remain relatively unchanged as they are not energetic enough to ablate and too massive for the atmosphere to decelerate. *Small, slow projectiles*: the mass of the atmospheric column becomes comparable to the mass of the object and deceleration occurs. *Fast projectiles*: deceleration and ablation are significant as the energy of traversing a column of atmosphere at a given velocity exceeds that required to ablate the entirety of its mass. The triangular wedge defines intermediate objects that would significantly ablate if deceleration does not occur, however deceleration limits the ablation. Model results of the ratios of initial and final (b) velocities and (c) masses are shown for projectile masses non-dimensionalized by the mass of the atmospheric column encountered on the *x*-axis and the initial projectile velocity squared by the energy per unit mass, σ^{-1}, on the *y*-axis. For $\sigma = 1 \times 10^{-8}$ kg J^{-1}, slow projectiles have $v_i < 10$ km s^{-1}, and for a 6 mbar martian atmosphere, small Ordinary Chondrite projectiles have diameters <10 cm.

distance, or, $dm \cdot \sigma^{-1} \propto \rho_a v^2 A \cdot v dt$. A transition to a high ablation regime will occur when the energy to ablate the entire meteoroid mass, $m \cdot \sigma^{-1}$, is equivalent to the energy required to traverse the atmosphere to the surface at a given velocity, $\rho_o HA \cdot v^2$, neglecting deceleration.

Using these criteria, we can classify the projectiles based on velocity and mass (Fig. 2). For large, slow projectiles, $m_f \sim m_i$ and $v_f \sim v_i$, and the projectile will reach the surface relatively unchanged. For smaller, slow objects where $m < \rho_o HA$, and $dm/dt \sim 0$, the final velocity decreases exponentially $v_f \sim v_i \exp\left[-\frac{\rho_a HA}{m \sin\theta}\right]$. Fast meteors, defined as having high initial velocities where $v_i^2 > \sigma^{-1}$, will experience significant ablation, $m_f < e^{-1} \cdot m_i$. Large, fast meteors will survive complete ablation if $m\sigma^{-1} < \rho_o HA \cdot v^2$, where the ablation will be limited by deceleration. These intermediate projectiles define the wedge shaped region in Fig. 2a. Our taxonomic boundaries are derived from our numeric modeling for a range of initial projectile masses and entry velocities (Fig. 2).

2.2. Monte Carlo simulation

We generated model crater populations using a Monte Carlo simulation employing the power-law distribution of observed meteoroid energies entering the top of the terrestrial atmosphere (Brown et al., 2002). These energies are converted to diameters and velocities assuming the normalized distribution of Earth encounter velocities for small impactor sizes from Marchi et al. (2009) and densities of the meteoroid materials observed from fireball networks (Ceplecha et al., 1998). The Moon/Earth impact flux ratio is taken to be 0.725 (Ivanov, 2006) to account for the gravitational capture cross sectional areas. The latest isochron model iteration of Hartmann (2005) assumes a scaling factor 2.6 for the nominal ratio of meteoroids at the top of Mars' atmosphere relative to the Moon and thus we assume a Mars/Earth ratio of 1.885. It should be noted that the factor 2.6 adopted by Hartmann is not well constrained and represents the largest uncertainty in the Hartmann isochrons. The distribution of entry velocities at Mars is taken to be (Bland and Smith, 2000; Davis, 1993; Flynn and McKay, 1990; Popova et al., 2003):

$$F(v_i) = 0.0231\, v_i \exp\left[-\left(\frac{v_i - 1.806}{8.874}\right)^2\right] \quad (5)$$

where $v_i \geqslant 5$ km s^{-1} (the escape velocity of Mars) with a mean velocity of 10.2 km s^{-1}. Following Love and Brownlee (1991), the probability distribution of entry angles is taken to be $\sin(2\theta)$, which has a maximum at 45° and drops to zero at 0° and 90°. The 5 meteoroid material types from Ceplecha et al. (1998) differ in their ability to penetrate the atmosphere, with the average ablation coefficient, σ, and bulk density, ρ_m, for each group listed in Table 1. We assume these average σ values; however, σ will vary with altitude and velocity. Model results for Ordinary Chondrites are shown in Fig. 3 for a single initial entry angle of 45°, demonstrating a good match with the results shown in Fig. 1.

Table 1
Distribution of material types based on fireball network observations (Ceplecha et al., 1998).

Group	% Obs.	Density, ρ_m (kg m^{-3})	Ablation coef., σ (s^2 m^{-2})
Irons	3	7800	7.0×10^{-8}
Ordinary Chondrites	29	3700	1.4×10^{-8}
Carbonaceous Chondrites	33	2000	4.2×10^{-8}
Cometary Material	26	750	10.0×10^{-8}
Soft Cometary Material	9	270	21.0×10^{-8}

The resulting crater volumes from the projectiles impacting the surface can be described by a scaling law that relates impact velocity and projectile and target characteristics (see Melosh (1989) for a review). In converting the crater SFD derived from the lunar surface to Mars, Hartmann (2005) assumes crater diameters, *D*, scale with impact energy as $E^{0.43}$ and with gravity as $g^{-0.17}$ to account for differences in mean impact velocity and gravitational acceleration between the two bodies. For small projectiles, the depth of excavation by an impact is small enough that lithostatic stresses are small relative to the characteristic yield stress of the regolith. In such cases the resulting transient crater diameter is determined by the yield strength, *Y*, of the target material ("strength scaling"), and no longer scales with gravity. The transition from strength scaling to gravity scaling occurs when $Y \sim \rho_t g R_p$ where R_p, the projectile radius, is taken to be the characteristic depth and ρ_t is the target density (Holsapple, 1993). For a regolith of density 2000 kg m^{-3} and yield strength of 0.1–1 MPa, the transition between strength and gravity dominated regimes occurs at $D \sim 27$–270 m on Mars. This implies that the 1–10 m scale fresh craters discovered by spacecraft over the last decade (Malin et al., 2006; Daubar et al., 2013) are predominately in the strength scaling regime. Strength scaling results in a reduction in crater volume relative to gravity scaled craters. As a consequence, the distribution of crater diameters would be expected to be shallower than that

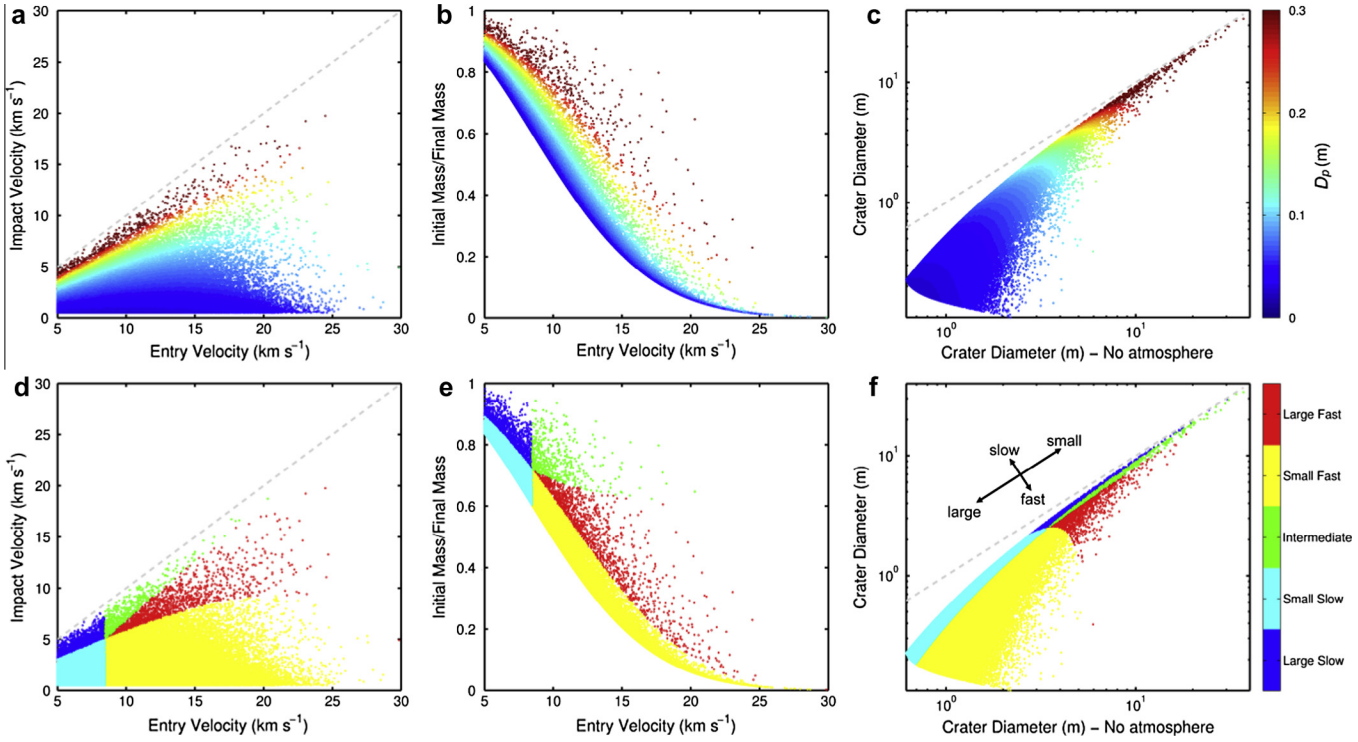

Fig. 3. Scatter plots of results from the Monte Carlo simulation with a bivariate distribution of velocities and projectile diameters for 2×10^5 events with initial entry angles 45° and ordinary chondritic compositions. (a) Impact velocity versus initial entry velocity, (b) initial and final mass ratio versus entry velocity, and (c) final crater diameter versus crater diameter without an atmosphere, i.e. crater diameter resulting from initial mass and velocity. The color scale of (a–c) shows the initial projectile diameter. (d–f) Are the same as (a–c) but events are tagged with 5 colors representing the general class of projectiles as defined in Fig. 2 (Slow/Fast, Small/Large). This trend is shown with arrows in (f). Deviations from the gray dashed lines in (a, c, d, and f), and from the horizontal in (b and e), show the magnitude of ablation and/or deceleration experienced by the objects. Crater diameters are determined assuming parameters of dry soil with effective strength, $Y = 65$ kPa and $\rho_t = 2000$ kg m^{-3} (Holsapple, 1993). (For interpretation of the references to colour in this figure legend, the reader is referred to the web version of this article.)

predicted by the isochrons of Hartmann (2005) at the smallest sizes, which assume all crater diameters scale with gravity.

The cratering efficiency, $\pi_v = \rho_t V/m_f$, where ρ_t is the target density and V is the transient crater volume, is proportional to (Holsapple, 1993):

$$\left(\pi_2 + \pi_3^{\frac{2+\mu}{2}}\right)^{-\frac{3\mu}{2+\mu}} \tag{6}$$

assuming impactor and target densities are the same, where μ is an empirical constant related to the target porosity ranging from 0.41 for relatively dissipative materials such as dry soils to 0.55 for rocks and wet soils. The parameters π_2 and π_3 are dimensionless numbers describing the cratering efficiency for gravity scaling and strength scaling, respectively, where $\pi_2 = gR_p/v_f^2$, the ratio of the lithostatic pressure at a depth equivalent to the projectile radius and the initial dynamic pressure generated by the impact, and $\pi_3 = Y/\rho_t v_f^2$, the ratio of effective target yield strength to the initial dynamic pressure (Holsapple, 1993). The vertical component of the final velocity, $v_f \sin\theta$ is used for non-vertical impacts. For smaller projectiles, the π_2 term becomes negligible and π_v becomes constant with impactor size, depending only on velocity and the material strength of the target. At large impactor sizes, π_2 dominates and the cratering efficiency is then dependent not only on velocity, but impactor size. The expression for transient crater volume is (Holsapple, 1993):

$$V_t = K_1\left(\frac{m_f}{\rho_t}\right)\left[\pi_2\left(\frac{\rho_m}{\rho_t}\right)^{\frac{1}{3}} + K_2\left(\pi_3^{\frac{2+\mu}{2}}\right)\right]^{-\frac{3\mu}{2+\mu}} \tag{7}$$

where K_1 and K_2 like μ and Y, are experimentally derived properties of the target material. The radius of the excavated crater is $R = K_r V_t^{1/3}$, where $K_r = 1.1$ for dry soils and soft rock materials and the final rim-to-rim diameter is taken to be 1.3 times the transient crater diameter (Holsapple, 1993). Note that the target material parameters in Table 1 of Holsapple (1993) have been updated (personal communication K. Holsapple) and published online: http://keith.aa.washington.edu/craterdata/scaling/theory.pdf. The values used in this study are summarized in Table 2: we adopt values for Mars consistent with dry desert alluvium with properties of "dry soils" (Table 2) with $Y = 65$ kPa and $\rho_t = 2000$ kg m^{-3} to account for alluvium rich in mafic minerals (Holsapple, 1993; Holsapple and Housen, 2007).

A minimum impact velocity threshold of 0.5 km s^{-1} is selected for the formation of explosive impact crater formation as projectiles with lower speeds are unlikely to generate a shock wave of sufficient magnitude to crush the target material and excavate an explosive crater (Popova et al., 2003). The definition of this velocity is not sharply defined and will depend on target material properties. Pressure wave velocities in competent basalt are typically ~4.5 to 6.5 km s^{-1}, with values an order-of-magnitude lower for loose, unconsolidated soils. Apollo seismic investigations found

Table 2
Impact crater scaling parameters.[a]

Material	K_1	K_2	μ	Y (MPa)	ρ_t (kg m^{-3})
Dry sand	0.132	0	0.41	0	1700
Dry soil	0.132	0.26	0.41	0.2	1700
Soft rock	0.095	0.215	0.55	1.0	2100
Hard rock	0.095	0.257	0.55	10.0	3200
Lunar regolith	0.132	0.26	0.41	0.01	1500

[a] Values from material published online (http://keith.aa.washington.edu/craterdata/scaling/theory.pdf) which supersede values in Table 1 of Holsapple (1993) (personal communication K. Holsapple).

velocities to be ~0.1 to 0.3 km s^{-1} in the upper 100 m of the lunar regolith (Kovach and Watkins, 1973; Watkins and Kovach, 1973).

The initial altitude of the modeled projectiles is 100 km. The gas density at this altitude is reduced by four orders-of-magnitude relative to the atmospheric density at the planet's surface, and thus deceleration (Eq. (1)) is reduced by four orders-of-magnitude relative to when the meteoroid is near the surface and is therefore initially negligible. This altitude also represents the approximate transition between the free molecular flow regime and the continuum regime (i.e. Knudsen number ~ 0.1, depending on the object size, for a mean free path of ~1 cm).

2.3. Aerodynamic breakup

The fragmentation of meteoroids during their flight through the atmosphere likely influences the resulting SFD of smaller diameter craters, as more than half (56%) of the >200 fresh craters observed by HiRISE are comprised of clusters of individual craters (Daubar et al., 2013). Numerous additional examples of crater clusters have been observed on the surface of Mars (Popova et al., 2007), implying that the fragmentation of meteoroids that penetrate deep into the atmosphere is a common phenomenon on Mars. The aerodynamic breakup of a projectile is expected when the dynamic pressure experienced during entry, $\rho_a v^2$, exceeds the bulk strength, σ_m, of the projectile. Bolides entering the terrestrial atmosphere display a wide range of strengths inferred from the broad range of observed breakup event altitudes with bulk strengths shown to be ~0.1 to 10 MPa (Ceplecha et al., 1998; Popova et al., 2011). The estimated bulk strengths are low compared to the tensile strength of recovered samples (typically 1–10%), implying fractures and other zones of weakness within the bodies determine bulk strength rather than material composition (Popova et al., 2011). Dynamic pressures experienced by projectiles entering the martian atmosphere will commonly exceed 1 MPa and therefore fragmentation should be expected, albeit at a lower altitude than observed in the terrestrial atmosphere.

Larger, faster objects experience greater dynamic pressure during flight (Fig. 4). Though there is no explicit size dependence on dynamic pressure, smaller objects begin to ablate and decelerate higher in the atmosphere, and therefore experience smaller peak loading at higher altitudes than larger objects. This implies a size dependence on fragmentation from entry dynamics alone. Further, it is anticipated that larger objects are inherently weaker as they likely contain a greater number of defects, and a power law relation based on statistical strength theory (Weibull, 1951) between bulk strength and sample mass is typically assumed in models (e.g. Artmieva and Shuvalov, 2001; Popova et al., 2003; Svetsov et al., 1995). However, recent analysis of meteorite fall observations in the terrestrial atmosphere suggests that, at least for stony objects, the relation between bulk strength and sample mass may be weaker (Popova et al., 2011). A possible size dependence on fragmentation was reported by Ivanov et al. (2010) based on a preliminary analysis of ~70 fresh craters, and is also exhibited by the 44 fresh craters observed by Daubar et al. (2013), 25 of which consist of two or more craters (57%). This percentage increases for craters with $D > 5$ m to 73% and decreases to 41% for craters with $D < 5$ m.

3. Results

3.1. Fragmentation

The effects of fragmentation on the crater SFD is explored with the model. We include aerodynamic break up of meteoroids in the simulation allowing fragmentation to occur when the dynamic pressure exceeds a threshold bulk strength, $\sigma_m = \rho_a v^2$ (Fig. 5). Fragmentation is assumed to occur as a single event; however, multiple fragmentation events at different points in a meteoroid's trajectory are sometimes observed during the flight of terrestrial fireballs. Catastrophic fragmentation (a point source type explosion with thousands of fragments) also occasionally occurs. We constrain the number of fragments to 2–100 and each fragment is followed individually to the termination of its flight in order to assess how fragmentation alters the resulting SFD. The maximum allowable number of fragments was selected because most observed clusters contain <100 craters (Daubar et al., 2010; Ivanov et al., 2010) and this value was found to be adequately large to characterize how fragmentation affected the resulting crater SFDs while remaining computationally feasible. The number of fragments generated is assumed to follow a power-law probability: we adopt a power-law slope of −1.5 for our nominal model and adjust this value to explore the sensitivity of our results on this exponent. Decreasing the power-law slope results in a more uniform distribution of fragment numbers (i.e. greater probability of getting events with a high number of fragments), while increasing the slope produces a distribution favoring events with fewer numbers of fragments. A cascade of fragment sizes is then generated by iteratively subtracting random mass fractions from the initial mass which typically

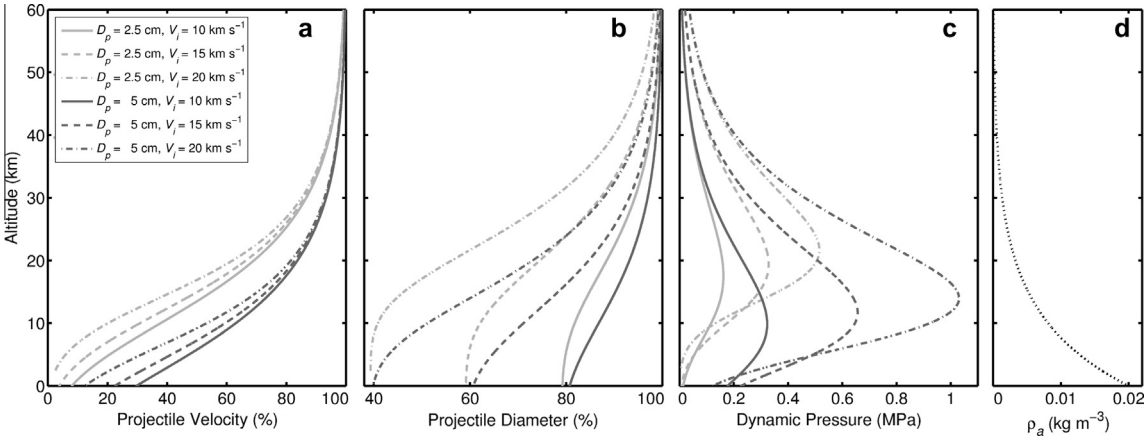

Fig. 4. Profiles of (a) the percent of initial velocity, (b) the percent of initial diameter, and (c) the dynamic pressure for six Ordinary Chondrites in the martian atmosphere as a function of altitude with entry angles 45°. (d) Assumed atmospheric density with altitude. Note that while the faster projectiles decelerate to a greater relative extent, they experience larger dynamic pressure upon entry. Ablation is more sensitive to velocity; however, deceleration is more sensitive to projectile size, and therefore smaller objects tend to experience lower dynamic pressures.

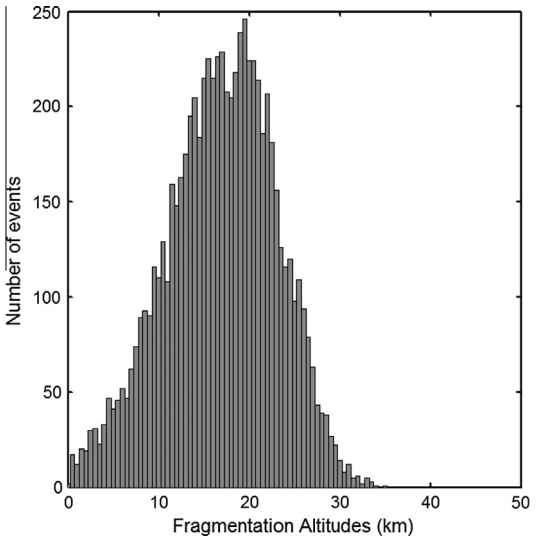

Fig. 5. Histogram of fragmentation altitudes using bulk strength $\sigma_m = 0.65$ MPa. Most fragmentation occurs ~2–3 scale heights above the surface with few fragmentation events occurring at lower altitudes. See Fig. 3 for the range of meteor sizes and velocities.

results in a small number of larger fragments and many smaller fragments. We additionally explore selecting mass fractions with a uniform random distribution of fragment sizes.

The model is run with 10^6 initial projectiles with a minimum allowable projectile diameter of 2 cm. A significant number of these events do not survive, but this minimum value was found to resolve the atmospheric downturn in the resulting crater SFD allowing the smallest permissible craters to form. The same bulk strength is selected for all the projectiles for simplicity (though there may be a weak correlation with strength and meteor type and size) and adjusted until the ratio of crater clusters to total impacts for $D > 5$ m is similar to the 73% observed for the 44 craters reported by Daubar et al. (2013). We find that a bulk strength of $\sigma_m = 0.65$ MPa best reproduces the observations, as shown in Fig. 6, which plots histograms in $\sqrt{2}$ bins of the resulting crater diameters. Both the observed and model craters are dominated by crater clusters at $D > 5$ m of approximately the same fraction. Effective diameters are estimated for the clusters by $D_{eff} = (\sum_i D_i^3)^{1/3}$, which represents the diameter of an equivalent crater due to a non-fragmented meteoroid (Malin et al., 2006; Ivanov et al., 2008).

There is a downturn in the SFD of the craters observed by Daubar et al. (2013) at $D \sim 4$–5 m. However, the model craters continue to increase in number at smaller diameter bins down to the $D = 0.24$ m bin in Fig. 6. The majority of craters have small diameters < 1 m, and the fraction of clusters in each bin becomes negligible, with the total fraction of all clusters comprising only 4% of the total model crater population. This implies that the atmospheric downturn has not been observed in the fresh craters, and that a significant number of craters with $D < 4$–5 m have not been identified. The discovery of fresh craters relies on the detection of dark spots in CTX images in dusty regions. A swarm of fragments will disturb a larger surface area creating, in general, larger dark spots. The predominance of single craters at $D < 5$ m indicates that detection will be more challenging as dark spots become inherently smaller relative to D at these sizes, partly explaining the downturn in the observed SFD at 4–5 m.

One might conclude that fragmentation, being only 4% of the events, may not be an important process in shaping the SFD. However, crater clusters begin to dominate the SFD at the very diameters that can be reliably detected by CTX, and therefore the effects on absolute ages derived from crater production functions are considered. Comparing the SFD of the model craters with craters produced by the same projectiles with fragmentation suppressed (Fig. 7), a difference in age of 7% is obtained when fitting the Hartmann (2005) production function for $D > 4$ m. The influence of fragmentation on the crater SFD can be increased by taking the probability of the number of fragments generated when σ_m is exceeded as random and uniform, instead of following the -1.5 slope power law, and a uniform distribution of fragment masses. In this case we obtain a factor ~0.69 difference in age relative to the age derived if no fragmentation is allowed to occur (Fig. 7b). This represents the model with fragmentation having the largest influence on the SFD that we consider.

The change in the crater SFD with fragmentation can be attributed to the mass dependence on ablation and deceleration as well as corresponding changes in crater scaling, which is not accounted for when calculating effective crater diameters, D_{eff}. Individual fragments experience greater deceleration and ablation per unit volume than the larger parent meteoroid. If enough of the total mass is shifted into a high deceleration/ablation regime when the parent object is broken into individual fragments, D_{eff} may no longer be representative of the crater generated by an equivalent unfragmented meteoroid. If the ratio of D_{eff} to the actual D resulting from the unfragmented projectile is $\ll 1$, then D_{eff} is a poor representation of the equivalent unfragmented crater. In general, $D_{eff}/D < 1$ when $D_{eff} \lesssim 10$ m for the nominal fragmentation case, with the potential reliability of D_{eff} decreasing with size (Fig. 8). Scatter in D_{eff}/D values is largely due to variations in meteoroid velocities with lower D_{eff}/D for faster objects. Some events result in D_{eff}/D

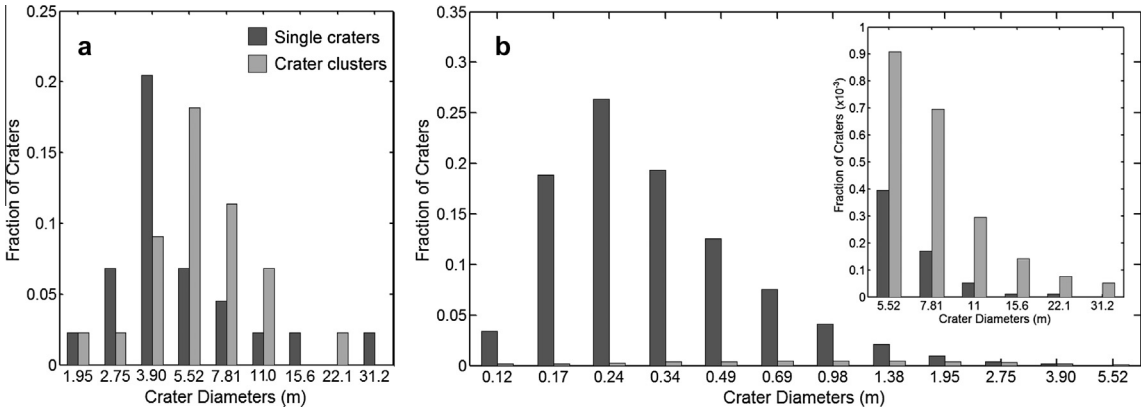

Fig. 6. Histograms of crater diameters for (a) the 44 fresh craters reported by Daubar et al. (2013) and (b) the model using bulk strength $\sigma_m = 0.65$ MPa. Diameters of crater clusters are effective diameters (see text). The inset is the model craters for $D > 5$ m.

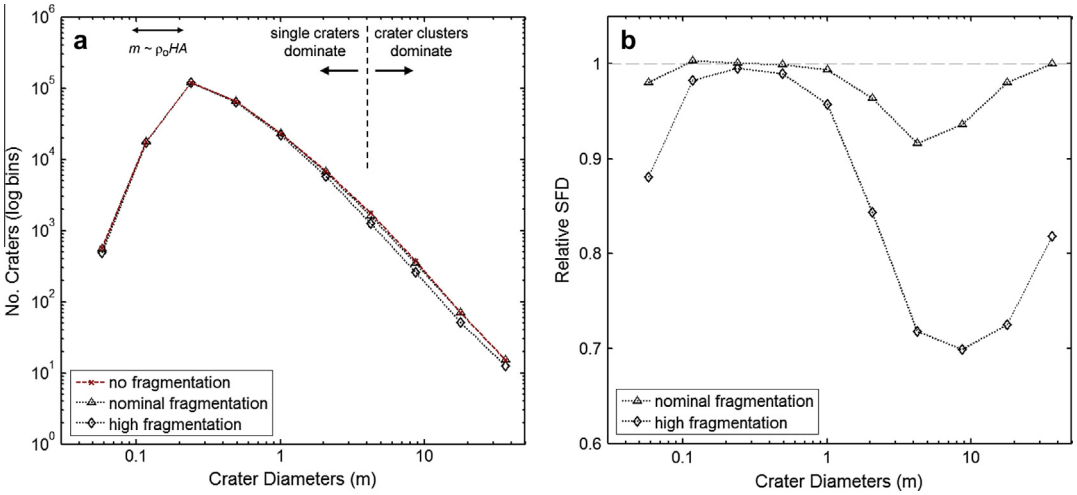

Fig. 7. (a) The modeled crater SFDs where no fragmentation occurs (i.e. $\sigma_m \gg \rho_a v^2$ for all meteoroids) and two different fragmentation characteristics: one favoring fewer fragments with few large fragments and many small fragments (nominal model), and one with a uniform random distribution of fragment numbers and sizes to increase the influence of fragmentation on the crater SFD. (b) The ratio of crater SFDs with and without fragmentation. The influence of fragmentation on the SFD is greatest at $D \sim 2$–20 m.

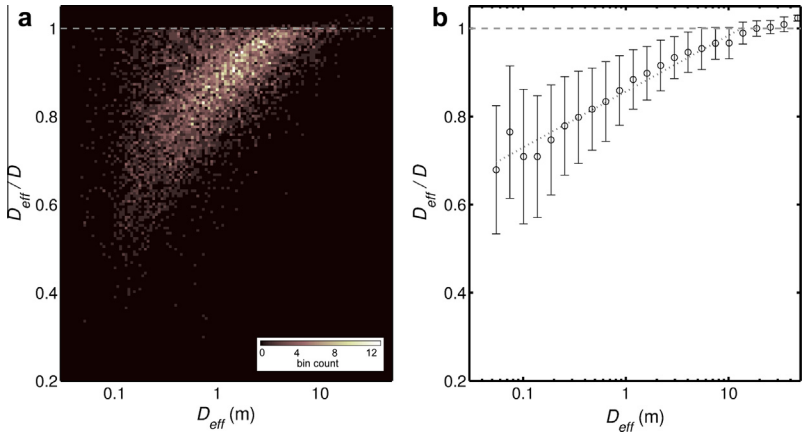

Fig. 8. (a) 2D histogram of model D_{eff}/D for individual crater clusters and (b) the mean in log D_{eff} bins. Error bars represent the standard deviation in each D_{eff} bin. D_{eff} is increasingly unreliable at smaller sizes below ~10 m. The dotted line is a fit to the mean values: $D_{eff}/D = 0.8568 + 0.1274 \log(D_{eff})$ for $D_{eff} = 5.5$ cm to 13.3 m.

values slightly greater than 1, predominately at $D_{eff} \gtrsim 10$ m, due to the dependence of impactor size on gravity scaling where crater efficiency decreases with increasing impactor size. Consequently, in some cases the crater efficiency can be larger for the fragments than for the parent projectile.

3.2. Impact-crater isochrons

The technique of dating the martian surface using predicted crater SFDs for well-preserved surfaces using impact-crater isochrons has been developed over several decades going back to the early lunar exploration of the 1960s (e.g. Hartmann, 1966, 1999, 2005; Neukum and Wise, 1976; Neukum and Ivanov, 1994; Hartmann and Neukum, 2001). Radiometric and exposure ages from Apollo and Luna samples, correlated with crater populations, have anchored the lunar cratering chronology. Scaling lunar isochrons for Mars to account for the ratio of meteoroids at the top of the martian atmosphere relative to the Moon and the difference in gravity and average impact velocity provides a means of understanding the absolute timescale of major geological and geophysical processes on Mars with order of magnitude accuracy. The Monte Carlo model is used to generate isochrons for Mars and the Moon with the ability to customize our isochrons. For example, we can develop an isochron for a specific elevation in the martian atmosphere or assumed target material properties.

An inflection at $D \sim 1.5$ km separates the isochrons into two branches with different power-law exponents. This inflection, initially observed in lunar craters, divides the crater distribution into a shallow branch with a slope of −1.80 and a steep branch of −3.82 on a log–differential plot. The range of energies used from Brown et al. (2002) restricts our isochrons to the steep branch of the SFD (i.e., $D < 1.5$ km). In his latest iteration of Mars isochrons, Hartmann (2005) included an atmospheric model (Popova et al., 2003) to encapsulate the effects of atmospheric entry of meteors resulting in curvature in the isochrons in the steep branch at sub-km crater diameters.

During impact, ejecta traveling large distances from a crater are capable of generating isolated secondary craters that could potentially be mistaken for primary craters. What fraction of observed crater populations are primary versus secondary, and the consequence of unidentified secondary craters in dating surfaces, is a matter of debate. McEwen et al. (2005), and McEwen and Bierhaus (2006), argue that small crater populations are dominated by secondary craters, rendering smaller craters unreliable for dating.

However, Hartmann (2005, 2007) points out that in formulating isochrons, no attempt is made to exclude all secondaries and contends that the accumulation of secondary craters are not "contamination" but rather part of the signal. A population of primary plus secondary craters will have a steeper SFD power law slope than a population devoid of secondary craters, and McEwen et al. (2005) has proposed that the increase in slope of the steep branch of crater SFDs is the result of secondaries.

Our approach of using the observed projectile production function at the top of the terrestrial atmosphere provides an opportunity to independently test the veracity of existing lunar and martian isochrons and explore how different factors can cause deviations in crater SFDs relative to these isochron models. We can also constrain the potential influence of secondary craters in these isochron models, as our Monte Carlo model only produces primary crater populations. If secondary craters are a substantial fraction of crater populations, then our model crater SFD should deviate in both slope and age from the isochrons. Additionally, since we use the present-day flux of projectiles, any significant deviation in age estimates can be attributed to a variation in average impact rate over time.

We test our model against crater counts conducted on the proximal ejecta of the crater Zunil (7.8°N, 166.1°E) and the impact melt deposit on the floor of Pangboche crater (17.2°N, 226.7°E). The crater Zunil is selected because it is likely the last $D = 10$ km scale crater to form on Mars (McEwen et al., 2005; Hartmann et al., 2010) with an estimated age of ~1 Ma based on the isochrons of Hartmann (2005), so the distribution of small craters on its ejecta

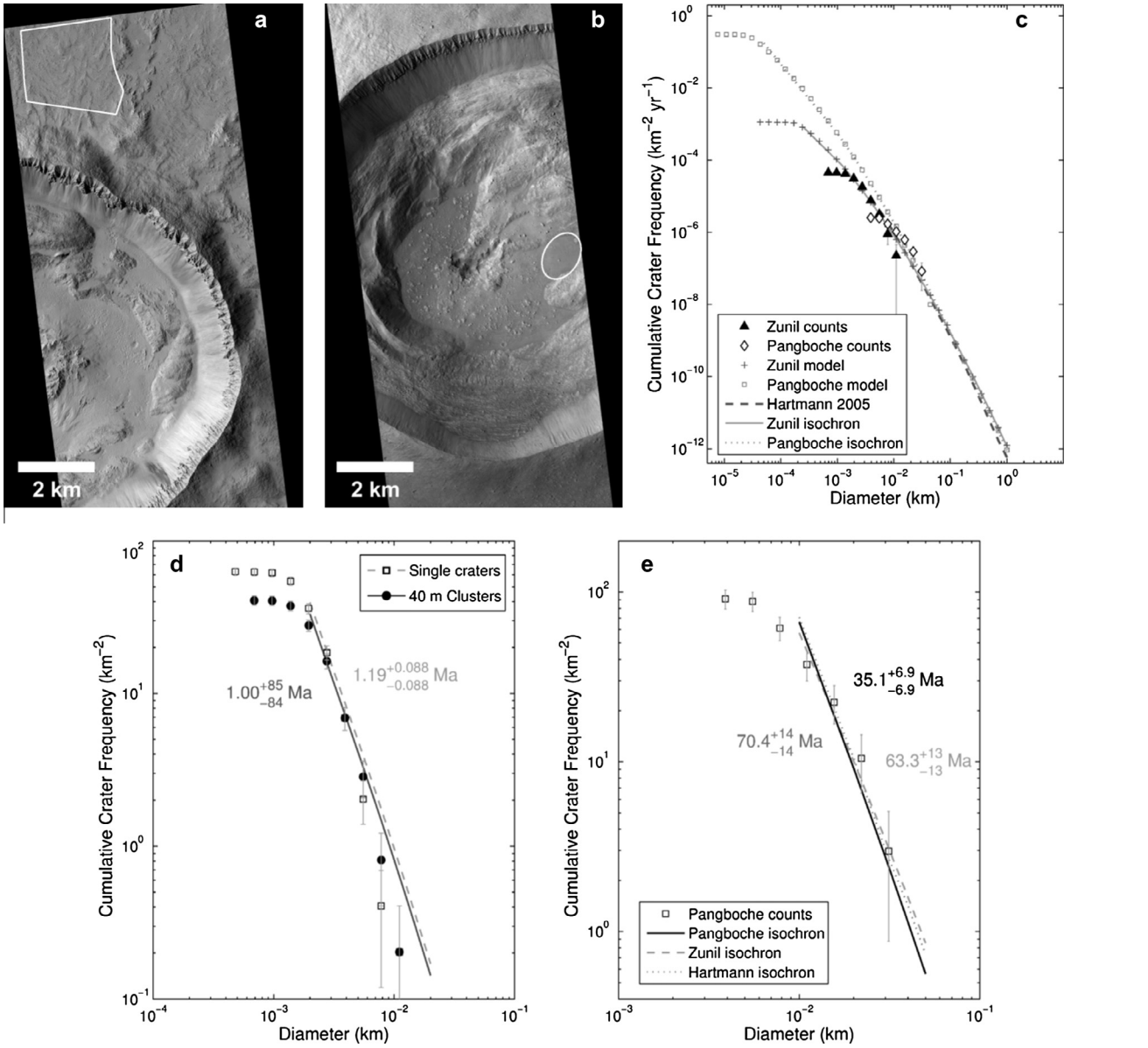

Fig. 9. Crater counts conducted on (a) ~5 km^2 area north of the Zunil crater rim using HiRISE image PSP_001764_1880 and (b) ~670 m^2 area on the floor of Pangboche crater using HiRISE image PSP_001643_1975, which were calibrated and map-projected using ISIS (Integrated Software for Imagers and Spectrometers) and imported into Arcmap, with CraterTools (Kneissel et al., 2011) used to identify and measure crater diameters. The count areas are outlined. (c) Modeled annual SFDs for the locations of Zunil and Pangboche craters and isochrons derived from polynomial fits. The crater counts from the two locations are scaled to the same time/area for comparison with the annual isochrons. (d) Zunil crater counts and ages estimated using the −2.8 km elevation (Zunil) model isochron. The two estimates shown assume each crater counted is an individual impact and that craters within 40 m proximity are part of a cluster. (e) Pangboche crater count with age estimates using the Hartmann isochron, the −2.8 km elevation model isochron, and the 20.8 km elevation model isochron. Data is binned in $\sqrt{2}$ diameter bins and ages estimated using the Craterstats2 tool (Michael and Neukum, 2010).

are likely to be predominately primary. Pangboche is selected because it is also a young crater, but likely an order-of-magnitude older than Zunil crater. Pangboche lies near the summit of Olympus Mons at an elevation of 20.8 km with a diameter of 10.8 km (comparable in size to Zunil). However, Pangboche lies at an elevation over two scale heights higher than Zunil with an atmospheric surface density an order-of magnitude lower. Pangboche has characteristics similar to younger lunar craters (Tornabene et al., 2012), including impact melt deposits on the crater floor, which have been attributed to the thinner atmosphere and lack of volatiles in the basaltic target (Osinski et al., 2011).

Crater counts were conducted on a ~5 km^2 area north of the crater rim of Zunil and a 670 m^2 area within the interior of Pangboche (Fig. 9). We then generate two model isochrons, one assuming a surface elevation of −2.8 km and one with an elevation of 20.8 km, the respective elevations of Zunil and Pangboche (Fig. 9c). With this approach, we can tailor isochron models to a location with a specific elevation or target property. The Zunil isochron model provides an age of 1.19 ± 0.088 Ma, similar to the ~1 Ma age estimated by Hartmann et al. (2010). If we assume craters within a 40 m proximity are part of a single cluster and convert them into effective diameters, then the SFD yields and age of 1.00^{+85}_{-84} Ma, a difference of 12.5%. The 40 m proximity criterion is somewhat *ad hoc* but results in a ~30% fragmentation rate. The fresh CTX craters display a fragmentation rate of 41% for $D < 5$ m and our model shows that rate of fragmentation decreases with D. Most of the observed craters on the Zunil ejecta are small with $D < 5$ m and therefore a proximity criterion with a 30% fragmentation rate for the range of D in our counts is likely reasonable for the purpose of comparison between using effective diameters and treating all craters as single events. Clusters are only identifiable when the densities of craters are low and clusters are spatially isolated. Once they start to form in close proximity to one another, the identification of individual clusters becomes more difficult and a simple proximity criterion should be used with caution. However, as our example demonstrates, treating all craters as single events will yield an older age.

The influence of the atmosphere on meter-scale craters can be seen by comparing the isochrons for Zunil and Pangboche, which diverge at $D \lesssim 10$ m (Fig. 9c), with the Zunil isochron having more downward curvature due to impactors having to penetrate deeper into the atmosphere to reach the surface. The curvature of the Hartmann isochron (which assumes a 6 mbar pressure atmosphere) closely resembles our Zunil-specific isochron, with both yielding similar age estimates for Pangboche: 63.3 ± 13 Ma using the Hartmann isochron and 70.4 ± 14 Ma using the Zunil isochron (Fig. 9e). However, our Pangboche-specific isochron, which accounts for the crater's higher elevation, yields an age estimate of 35.1 ± 6.9 Ma. Hence, at the summit of Olympus Mons, failure to account for the effects of altitude upon small crater production will result in an over estimation of surface age by a factor of ~2.

We also compare our isochrons with the 19 fresh MOC (Malin et al., 2006) and 44 fresh CTX–CTX detected craters (Daubar et al., 2013). The crater SFDs are scaled to an equivalent time/area for comparison (Fig. 10). The fresh craters fall below the isochron as noted by Daubar et al. (2013). The largest CTX crater, $D = 33.8$ m, is consistent with a single $D \sim 30$ m crater predicted to form annually for the scaled observation area. However, smaller diameter bins are inexplicably under-populated relative to that predicted by the isochron models, resulting in a shallower power law slope. Note that the atmospheric downturn is expected to occur at much smaller diameters (sub-meter), and fragmentation will not substantially deplete the SFD at these smaller sizes (Fig. 6b). A lack of a contribution from secondaries to the isochrons also cannot explain the discrepancy, as our model generates a primary-only SFD.

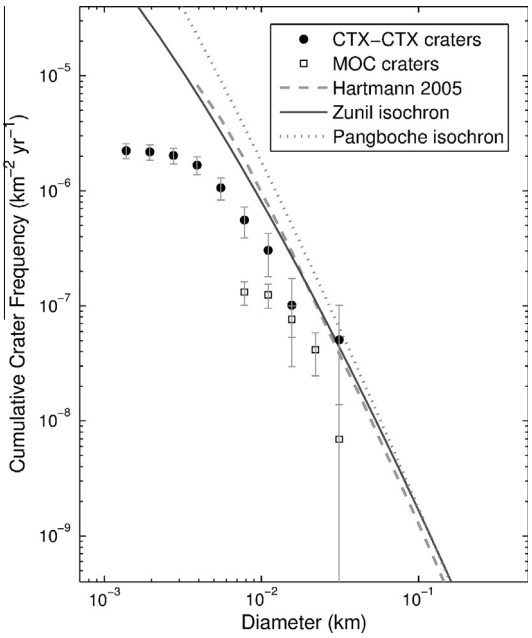

Fig. 10. The cumulative SFD for the fresh craters from CTX–CTX detections (Daubar et al., 2013), and MOC observations (Malin et al., 2006), binned in $\sqrt{2}$ diameter bins, and the isochron model of Hartmann (2005) and isochrons derived from our model for surface elevations of −2.8 km (Zunil) and 20.8 km (Pangboche), scaled to the same time/area.

Fresh craters discovered using MOC also have an apparent deficit of craters at all bin diameters. The MOC camera, with a lower resolution, did not detect any craters below $D \sim 10$ m and detected fewer craters in all bin sizes that overlap with the CTX craters. All bin sizes (except for the largest CTX crater) fall below the isochrons, and this discrepancy is greater in the lower resolution dataset. This indicates that observational bias may be the best explanation for the difference between the isochrons and the observed SFDs. Since larger craters are more likely to create detectable dark spots on the surface, the observation of larger diameter craters in the future by CTX/HiRISE, given a longer observational baseline, has the potential to resolve whether this discrepancy is real or not. If the SFD start to overlap with the model isochrons at the larger diameter bins, then an observational bias at smaller crater diameters would be implied. This would then suggest that fresh craters were undercounted by MOC at all diameters observed. If however the shallower slope persists, this might indicate that differences exist between the present-day population of observed objects colliding with the Earth and Mars. A single value for the Mars/Moon impactor ratio is assumed by Hartmann (2005); however it is possible that this ratio actually has a diameter dependence (Shane Byrne, personal communication). If so, the fact that we are able to reproduce the slope of the SFD of craters on the ejecta of Zunil then would be coincidental and would imply a population of secondary craters are compensating for a different primary SFD.

3.3. Lunar crater counts

As an additional test, we compare results from the model with crater counts of small craters on the Moon (Fig. 11). The ejecta of North Ray and Cone craters were selected for their relatively young age, which has been constrained by cosmic ray exposure ages of samples from Apollo 16 (50.3 ± 0.8 Ma) and Apollo 14 (25.1 ± 1.2 Ma) respectively (Arvidson et al., 1975; Stöffler and Ryder, 2001). Our small (0.1 km^2) study areas only contain craters $D \leqslant 22$ m. Applying the cratering chronology of Neukum et al. (2001), ages of 58.9 ± 11 Ma (North Ray) and 27.9 ± 9.2 Ma (Cone)

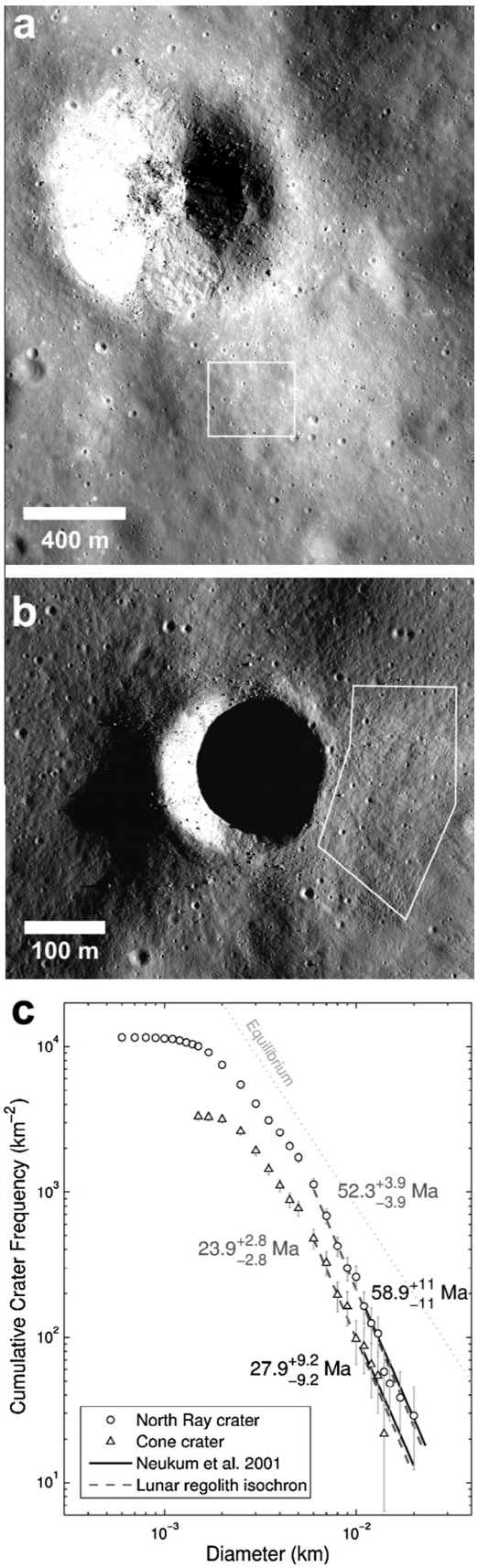

Fig. 11. (a) Location of North Ray crater count area in Lunar Reconnaissance Orbiter Camera (LROC) NAC image M129187331 and (b) Cone crater count area in LROC NAC image M162426054 (NASA/GSFC/ASU). (c) The cumulative crater frequency of the crater counts and ages estimated using the Neukum et al. (2001) isochron and our model isochron.

are derived from the resulting cumulative SFDs. Counts by Hiesinger et al. (2012) yield a similar age for North Ray crater using a larger, but overlapping area.

We generated isochrons for small craters on the Moon using our same general approach for Mars, but without an atmosphere. The distribution of encounter velocities of Marchi et al. (2009) is assumed, as are crater scaling parameters appropriate for the lunar regolith (Table 1). The isochron from the resulting SFD of the Monte Carol model results in ages of 52.3 ± 3.9 Ma for North Ray crater and 23.9 ± 2.8 Ma for Cone crater (Fig. 11).

Moore et al. (1980) measured power-law slopes of −2.8 and −2.7 at North Ray and Cone craters (respectively) from SFDs of small, 5–50 m diameter craters. However, the steep branch of the lunar crater SFD estimated by Hartmann and Gaskell (1997) is −3.82 based on an average of four sets of crater data measured in the lunar maria. McEwen and Bierhaus (2006) argue that this discrepancy is evidence of the existence of secondary craters in the lunar crater counts used to determine the steep branch. However, this −3.82 slope for the steep branch was only measured down to $D \sim 250$ m, since craters saturate at smaller sizes in the lunar maria. By including counts on young lunar surfaces and asteroids, Neukum et al. (2001) defines an isochron that extends down to $D = 10$ m. Neukum et al.'s isochron deviates from the −3.82 slope for $D < 250$ m and has a slope of −3.0 for $D = 10$–23 m, which is the diameter range we fit to our counts in Fig. 11. Our model isochron has a similar slope, −3.1, over the same diameter range. The slope of our counts derived from a maximum-likelihood estimation is −2.8 and −2.9 for North Ray and Cone, respectively, consistent with Moore et al. (1980).

This demonstrates the usefulness of our approach, as we are able to reproduce ~25 and ~50 Ma surface ages on the Moon using two limited areas containing only small craters. If craters in these areas were predominately secondary craters at these diameters, then our Monte Carlo models should have predicted much younger surface ages and a shallower slopes. In other words, we would need to run our models longer to match the populations of craters comprised of primaries and secondaries. A similar approach was taken by Ivanov (2006) to demonstrate that small craters on the Moon must be predominately primaries on young surfaces (⩽100 Ma), consistent with our model.

Our ability to reproduce isochron ages using a small area with a limited range of diameters imply that small craters can provide useful information about surface ages <50 Ma in age, and also indicates that the cratering rate has on average been relatively constant over this period (Ivanov, 2006). A lower impact rate in the past coupled with a secondary contribution could in principle produce a similar age, but would be expected to result in a different power-law exponent. That our counts and model isochrons have similar slopes implies this is not the case. Neukum and Ivanov (1994) showed that the crater SFDs in the diameter range 20 m to 1 km on the Moon spanning 0.1–3 Ga coincide and can be normalized to a single function, indicating that there is no significant variation with time in the crater SFD. The impact rate on Mars is complicated by variations in orbital eccentricity and its closer proximity to the asteroid belt and likely has not been constant in time. How secondary craters alter the SFD and whether such small craters can be reliably used for age dating surfaces in all cases is beyond the scope of this work, but our Monte Carlo approach does independently confirm that crater-count chronometry systems can accurately date the youngest surfaces on the Moon and, making assumptions regarding the Mars/Moon impact ratio, Mars.

3.4. Sensitivity analysis

The sensitivity of our results to changes in model parameters is evaluated (Table 3). Our nominal case overlaps with the Hartmann

Table 3
Sensitivity analysis.

Model (1 yr)	Best-fit[a] isochron from Hartmann (2005)	
	D = 4–20 m	D = 20–100 m
Nominal	0.769 ± 0.001	1.13 ± 0.010
Highlands (ρ_o = 0.0135 kg m^{-3})	0.722 ± 0.013	1.07 ± 0.003
Lowlands (ρ_o = 0.0222 kg m^{-3})	1.02 ± 0.015	1.30 ± 0.003
$\sigma \times$ ½	1.09 ± 0.016	1.38 ± 0.004
$\sigma \times 2$	0.512 ± 0.011	0.856 ± 0.003
Ordinary Chondrite only	1.68 ± 0.010	1.88 ± 0.004
Carbonaceous Chondrite only	0.701 ± 0.013	1.21 ± 0.004
Cometary Material only	0.161 ± 0.0001	0.481 ± 0.002
Dry sand	2.34 ± 0.023	2.85 ± 0.005
Lunar regolith	1.29 ± 0.017	1.58 ± 0.004
Soft rock	0.228 ± 0.0002	0.401 ± 0.002
Hard rock	0.071 ± 0.0001	0.113 ± 0.001
R_{bolide} = 3.3	0.968 ± 0.015	1.43 ± 0.004
R_{bolide} = 1.9	0.586 ± 0.012	0.826 ± 0.003

[a] Isochrons fit to cumulative SFD using Craterstats2 program (Michael and Neukum, 2010).

(2005) annual isochron with a slightly shallower power-law slope, with the model producing a SFD that results in an age of 1.13 ± 0.01 yr for D = 20–100 m and 0.769 ± 0.001 yr for D = 4–20 m (Fig. 12). This slope difference could be the result of greater atmospheric influence on the meteoroids at smaller sizes than predicted by the atmospheric model of Popova et al. (2003) that is incorporated into the isochron, or could be due to Hartmann (2005) assuming gravity scaling only which would also result in less downturn in the isochron as crater scaling transitions into the strength regime (Section 2.2).

The mass of the atmospheric column that a meteoroid must traverse will depend on the location of the event, as the elevation of the surface can vary substantially. The highest elevation, the summit of Olympus Mons, is ~21 km above the global average datum, while at the other extreme, the interior of Hellas Basin, is ~8 km below. This represents a range of over 2.5 atmospheric scale heights. One of the most striking characteristics of martian topography is that its distribution is bimodal due to the north–south dichotomy in crust thickness (Smith et al., 1999). The more heavily cratered highlands in the southern hemisphere have an average elevation of ~1.5 km while the distribution of lowland elevations narrowly peak ~5.5 km lower than the highlands (Aharonson et al., 2001). This translates to an increase in average atmospheric density at the surface by a factor 1.6 between the southern highlands, ρ_o = 0.0135 kg m^{-3}, and the northern lowlands, ρ_o = 0.0222 kg m^{-3}. Taking the same model projectiles and generating craters for the two average elevations of the highlands and lowlands, two crater SFDs are generated for comparison (Fig. 12b). Craters $D \geqslant 20$ m result in ages 1.30 yr and 1.07 yr respectively, bracketing the nominal model results. This is a change of +15.0% and −5.3%. Fitting the smaller diameters, D = 4–20 m, results in ages 1.02 yr and 0.722 yr, a change of 32.6% and −6.1%. The greater sensitivity at the small crater diameters is to be expected as smaller projectiles are more sensitive to atmospheric conditions.

Increasing and decreasing the ablation coefficients, σ, has a similar effect as changing the atmospheric surface density, as an increase in the rate of mass loss results in smaller objects which in turn results in greater deceleration. Models for the same projectiles with ablation coefficients half the nominal values and double the nominal values were run (Fig. 12c). The derived ages for craters $D \geqslant 20$ m increased by 22.1% and decreased by 24.2% for $\sigma \times 1/2$ and $\sigma \times 2$ respectively, and similarly for craters D = 4–20 m increased by 41.7% and decreased by 33.4%.

The model assumes that the different taxonomic types of fireballs distinguished from the larger Earth-entering meteoroids (Ceplecha et al., 1998; Popova et al., 2003) have the same fractional distribution at Mars. These types of fireballs differ in their ability to penetrate the atmosphere and therefore if the proposed fractions of projectiles are substantially different on average from that observed in the terrestrial atmosphere (Ceplecha et al., 1998), the results will change. For example, a greater percentage of higher density objects will experience less deceleration and result in larger craters for a given population of projectiles. The smallest craters in the simulation, cm-scale, are formed exclusively by iron objects due to their high density (7800 kg m^{-3}). Iron meteors however are a small fraction of the total population (3%). The majority of the objects are Ordinary Chondrites (29%), Carbonaceous Chondrites (33%), and Cometary Material (26%). None of the Soft Cometary Material objects, with a density of 270 kg m^{-3}, survive passage through the martian atmosphere. To demonstrate the sensitivity of the model results to different projectile compositions, we run the simulation assuming pure compositions of the three predominant types: Ordinary Chondrites, Carbonaceous Chondrites, and Cometary Material (Fig. 12d). The Ordinary Chondrites, with a density greater than the average combined density, results in a factor >2 increase in age, while the Carbonaceous Chondrites produce a similar age reduced by only 8.8% for D = 4–20 m and increased by 7.1% for $D \geqslant 20$ m. A meteor population comprised entirely of Cometary Material results in substantially younger age estimates, 0.161 and 0.481 yr for the small and large diameters respectively, younger than the ages derived from either the MOC or CTX–CTX craters, with a slope that deviates from the isochron increasingly at smaller D. The crater counts from Zunil in Fig. 9c are shown in Fig. 12 for comparison, scaled to the 1 yr isochron, showing a slope consistent with a population of objects with average density similar to the nominal values assumed and inconsistent with a substantial fraction of icy, low-density impactors.

The crater scaling becomes increasingly sensitive to the target material properties as projectile diameters decrease with weaker material producing a larger crater for a given projectile. Details of the target properties, particularly the effective strength, may not be well constrained and can vary by location, feature, or geologic unit. Dundas et al. (2010) has demonstrated how this can complicate geologic interpretation as surfaces of the same age, but differing material properties, may yield different ages. We explore the sensitivity of the model to a range of target properties. Fig. 12e shows the results for the same population of projectiles for four different targets from Holsapple (1993) and summarized in Table 2. We take dry sand and the lunar regolith of Section 3.3 as reasonable weaker target materials and soft rock and hard rock for two targets with greater strength and density than our nominal Mars regolith. For the rock materials, μ = 0.55, the higher value reflecting lower porosity and therefore less energy dissipation (Holsapple and Housen, 2007). The hard rock gives an upper bound representative of competent, young basalt that lacks a substantial regolith cover.

The discrepancy in ages between resulting crater SFDs of the different target materials increases as much as a factor 3 for the dry sand and decreases by a factor of 2.4 for the hard rock. The stronger rock materials yield smaller craters and the corresponding decrease in estimated ages can results in SFDs that overlap with the observed CTX–CTX and MOC fresh craters (Fig. 12e). For our model to be consistent with the SFD of the fresh craters, the majority of the craters would have to have formed in relatively strong, competent rock. Many of the craters are on Amazonian units in the Tharsis region which is dominated by Amazonian lava flows; however, the largest CTX crater, D = 33.8 m, formed on the southeast flank of Pavonis Mons on a relatively young Amazonian volcanic unit (Scott et al., 1998). This crater is consistent with Hartmann (2005) which predicts an annual $D \sim 30$ m diameter crater and its presence in the fresh crater population cannot be attributed to the crater having formed in weaker target material relative to the other

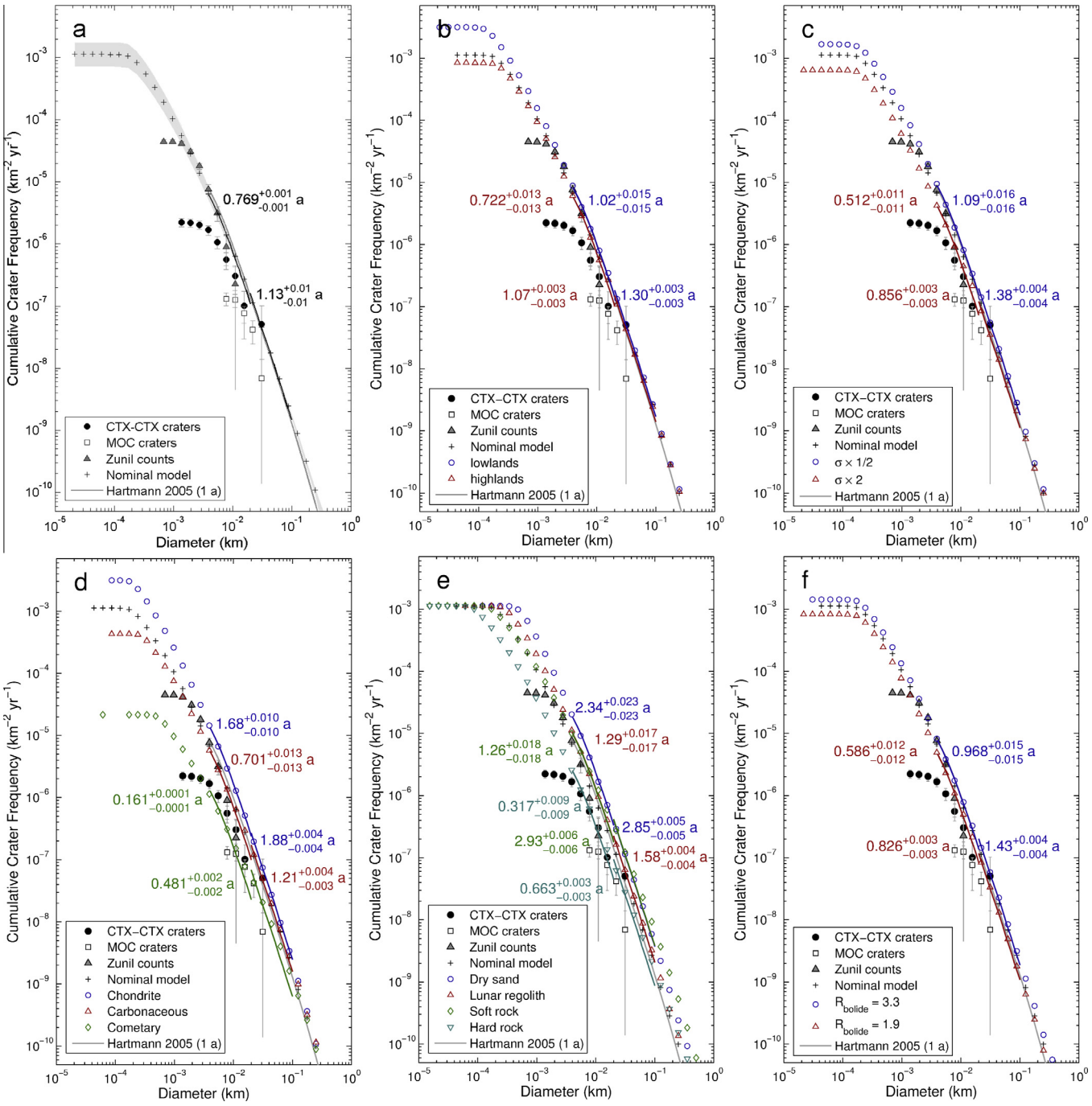

Fig. 12. Sensitivity of cumulative SFD to model parameters. (a) Nominal Zunil model, fresh craters identified with MOC (Malin et al., 2006), and CTX (Daubar et al., 2013), and counts conducted on Zunil ejecta scaled to an annual isochron of Hartmann (2005). Estimated ages are for D = 4–20 m and D = 20–100 m. Nominal model assumes: elevation of Zunil crater (−2.8 km), the distribution of meteoroid types with corresponding ablation coefficients as given by Ceplecha et al. (1998), and target material properties consistent with dry desert alluvium, K_1 = 0.132, K_2 = 0.26, μ = 0.41, ρ = 2000 kg m^{-3} and Y = 65 kPa. Gray shading shows range of model results accounting for uncertainty in parameters a_o = 0.5677 ± 0.015, and b_o = 0.90 ± 0.03 in the cumulative number of bolides colliding with the Earth per year with energies of E and greater (Brown et al., 2002): $\log(N) = a_o - b_o \log(E)$. (b) Results for average elevations of the Highlands and Lowlands. (c) Results scaling the ablation coefficients, σ, by 0.5 and 2. (d) Results assuming all projectiles made of Ordinary Chondrites, Carbonaceous Chondrites, or Cometary Material as defined in Table 1. (e) Results assuming target material properties of dry sand, lunar regolith, soft rock, and hard rock. (f) Results assuming Hartmann (2005) range of estimated uncertainty in the Mars/Moon impactor flux, R_{bolide} = 2.6 ± 0.7.

fresh craters. It is tempting to dismiss the single crater as a statistical outlier. However, it is incorrect to interpret the $\sqrt{n}$ error bars in comparison to model isochrons as these error bars indicate the 1–σ range of likely *observations* not *models*. That is, in an additional observation year, no new events of this size may occur; but the real flux of events of this size cannot be 0 given that a single event has been observed. Hence, models with low formation rates are unlikely given this observation (Aharonson, 2007).

The scaling factor assumed by Hartmann (2005) for the ratio of meteoroids at the top of the martian atmosphere relative to the Moon, R_{bolide}, is estimated to be 2.6 ± 0.7. Fig. 12f shows the resulting age estimates taking Hartmann's estimated range of uncertainty for R_{bolide} of ±0.7. This translates into an approximately ±25% variation in estimated age.

If continued observations of fresh CTX–CTX craters verify that the current observed SFD is indeed an accurate reflection of the

present-day impact crater population, then our model demonstrates that it is possible to constrain the fraction of impactor material types and average target material properties for Mars. For example, a population of impactors with average densities similar or higher than that observed for terrestrial fireballs could be ruled out as they are not consistent with the current CTX–CTX observations.

4. Discussion

The fact that the slopes of the Neukum et al. (2001) and Hartmann (2005) isochrons are similar to the isochrons derived in our study using the present-day annual flux of terrestrial fireballs implies that the isochron systems do not incorporate many unrecognized secondary craters at the locations we studied. This is quite unexpected considering McEwen et al. (2005) identify $\sim 10^7$ secondary craters generated by the Zunil crater forming impact event at distances up to 3500 km away from the primary crater. This implies that small secondaries should be abundant on the martian surface. We specifically selected young surfaces to conduct counts that likely reflect a primary crater population so it is not surprising that our counts have similar slopes to our model. The isochron system for $D > 250$ m is derived from counts conducted on lunar maria with average ages of 3.5 Ga, surfaces that have had ample time to accumulate secondaries. The isochron models at small diameters are derived from young lunar surfaces, which possibly have not accumulated a substantial population of unrecognized distant secondaries. Perhaps secondaries dominate on older Ga surfaces at these small diameters, but are saturated, and therefore the contribution of secondaries to the SFD is not observable and thus not as relevant to isochron models. Contamination by secondary craters is very heterogeneous in time and space and therefore the reliability of derived ages may be difficult to determine. We have not attempted a systematic survey to identify a range of crater diameters and surface ages where secondaries are influencing the crater SFD, which is beyond the scope of this study. Nevertheless, the compelling evidence for the existence of large numbers of secondaries (McEwen et al., 2005) implies caution must be taken in using small craters to age-date surfaces as this remains an unresolved issue. However, we have demonstrated that small crater populations on young surfaces that are unlikely to be contaminated by secondaries contain useful information about surface ages.

5. Conclusions

Taking the size distribution of the observed annual flux of terrestrial fireballs, the nominal Mars/Moon ratio of 2.6 for Mars employed by Hartmann (2005), and appropriate encounter velocity distributions for Mars and the Moon, we are able to generate crater populations with a remarkably similar SFD to that predicted by the isochrons of Hartmann (2005) for Mars and Neukum et al. (2001) for the Moon. Our Monte Carlo model generates a population of primary craters, implying that the isochrons do not contain a significant secondary crater signal in the range of crater diameters studied here since large numbers of secondaries would result in steeper isochron slopes and younger surface ages than predicted by our model. This further implies that the inflection from the shallow branch to the steep branch is not attributable to the addition of unidentified secondary craters. Crater counts conducted at Zunil and Pangboche on Mars and North Ray and Cone crater on the Moon yield SFDs with similar slopes as our model isochrons, and we derive similar ages as sample dating for the Moon demonstrating that the average cratering rate has been fairly constant on these bodies over these time periods.

We find that the details of the atmospheric model for Mars do not substantially alter the results. The Hartmann (2005) isochrons include an atmospheric model (Popova et al., 2003), and differences between the lowlands and highlands do not result in significant deviations from the Hartmann isochron, nor do variations in assumed ablation coefficients. Fragmentation did not significantly alter the model results and smaller projectiles ($D < 5$ m) typically were decelerated enough to avoid fragmentation. The atmospheric downturn predicted by our model occurs at $D \sim 10$–20 cm, corresponding to projectile masses roughly equivalent to the mass of the atmospheric column the objects are traversing. This is well below the downturn observed in the fresh craters detected by CTX at $D = 4$–5 m (Daubar et al., 2013), which we suggest is likely due to CTX detection limits. Continued observation may potentially resolve this question.

Acknowledgments

J.-P.W. and A.P. were supported by a NASA Mars Data Analysis Program Grant No. NNX11AQ64G. We thank Shane Byrne and an anonymous reviewer for their helpful reviews which improved the manuscript and Re'em Sari for his insightful comments and discussion.

References

Aharonson, O., 2007. The modern impact cratering flux at the surface of Mars. Lunar Planet. Sci. 38, #2288.
Aharonson, O., Zuber, M.T., Rothman, D.H., 2001. Statistics of Mars' topography from the Mars Orbiter Laser Altimeter' Slopes, correlations, and physical models. J. Geophys. Res. 106, 23723–23735.
Artmieva, N.A., Shuvalov, V.V., 2001. Motion of a fragmented meteoroid through the planetary atmosphere. J. Geophys. Res. 106, 3297–3309.
Arvidson, R., Crozaz, G., Drozd, R.J., Hohenberg, C.M., Morgan, C.J., 1975. Cosmic ray exposure ages of features and events at the Apollo landing sites. Moon 13, 259–276.
Baldwin, B., Sheaffer, Y., 1971. Ablation and breakup of large meteoroids during atmospheric entry. J. Geophys. Res. 76, 4653–4668.
Basilevsky, A.T. et al., 2009. Episodes of floods in MangalaValles, Mars, from the analysis of HRSC, MOC and THEMIS images. Planet. Space Sci. 57, 917–943.
Bland, P.A., Smith, T.B., 2000. Meteorite accumulations on Mars. Icarus 144, 21–26.
Bronshten, V.A., 1983. Physics of Meteoric Phenomena. Reidel, Dordrecht, 356p..
Brown, P., Spalding, R.E., ReVelle, D.O., Tagliaferri, E., Worden, S.P., 2002. The flux of small near-Earth objects colliding with the Earth. Nature 420, 294–296.
Burr, D.M., Grier, J.A., Keszthelyi, L.P., McEwen, A.S., 2002. Repeated aqueous flooding from the Cerberus Fossae: Evidence for very recently extant, deep groundwater on Mars. Icarus 159, 53–73.
Byrne, S. et al., 2009. Distribution of mid-latitude ground ice on Mars from new impact craters. Science 25, 1674–1676.
Ceplecha, Z. et al., 1998. Meteor phenomena and bodies. Space Sci. Rev. 84, 327–471.
Chyba, C.F., Thomas, P.J., Zahnle, K.J., 1993. The 1908 Tunguska explosion – Atmospheric disruption of a stony asteroid. Nature 361, 40–44.
Daubar, I.J., McEwen, A.S., 2009. Depth to diameter ratios of recent primary impact craters on Mars. Lunar Planet. Sci. 40, #2419.
Daubar, I.J., Byrne, S., McEwen, A.S., Kennedy, M., 2010. New Martian Impact Events: Effects on Atmospheric Breakup on Statistics. 1st Planetary Cratering Consortium.
Daubar, I.J. et al., 2011. New craters on Mars and the Moon. Lunar Planet. Sci. 42, #2232.
Daubar, I.J., McEwen, A.S., Byrne, S., Kennedy, M.R., Ivanov, B., 2013. The current martian cratering rate. Icarus 225, 506–516.
Davis, P.M., 1993. Meteoroid impacts as seismic sources on Mars. Icarus 105, 469–478.
Dundas, C.M., Byrne, S., 2010. Modeling sublimation of ice exposed by recent impacts in the martian mid-latitudes. Icarus 206, 716–728.
Dundas, C.M., Keszthelyi, L.P., Bray, V.J., McEwen, A.S., 2010. Role of material properties in the cratering record of young platy-ridged lava on Mars. Geophys. Res. Lett. 37, L12203. http://dx.doi.org/10.1029/2010GL042869.
Flynn, G.J., McKay, D.S., 1990. An assessment of the meteoritic contribution to the martian soil. J. Geophys. Res. 95, 14497–14509.
Hartmann, W.K., 1966. Martian cratering. Icarus 5, 565–576.
Hartmann, W.K., 1999. Martian cratering VI: Crater count isochrons and evidence for recent volcanism from Mars Global Surveyor. Meteorit. Planet. Sci. 34, 167–177.
Hartmann, W.K., 2005. Martian cratering 8: Isochron refinement and the chronology of Mars. Icarus 174, 294–320.

Hartmann, W.K., 2007. Martian cratering 9: Toward resolution of the controversy about small craters. Icarus 186, 274–278.
Hartmann, W.K., Berman, D.C., 2000. Elysium Planitia lava flows: Crater count chronology and geological implications. J. Geophys. Res. 105, 15011–15025.
Hartmann, W.K., Gaskell, R.W., 1997. Planetary cratering 2: Studies of saturation equilibrium. Meteorit. Planet. Sci. 32, 109–121.
Hartmann, W.K., Neukum, G., 2001. Cratering chronology and evolution of Mars. In: Altwegg, K., Ehrenfreund, P., Geiss, J., Huebner, W.F. (Eds.), Composition and Origin of Cometary Materials. Kluwer Academic, The Netherlands, pp. 165–194.
Hartmann, W.K., Quantin, C., Werner, S.C., Popova, O., 2010. Do young martian ray craters have ages consistent with the crater count system? Icarus 208, 621–635.
Hiesinger, H. et al., 2012. How old are young lunar craters? J. Geophys. Res. 117, E00H10. http://dx.doi.org/10.1029/2011JE003935.
Holsapple, K.A., 1993. The scaling of impact processes in planetary science. Annu. Rev. Earth Planet. Sci. 21, 333–373.
Holsapple, K.A., Housen, K.R., 2007. A crater and its ejecta: An interpretation of Deep Impact. Icarus, 345–356.
Ivanov, B.A., 2006. Earth/Moon impact rate comparison: Searching constraints for lunar secondary/primary cratering proportion. Icarus 183, 504–507.
Ivanov, B., Melosh, H.J., McEwen, A.S., and the HiRISE team, 2008. Small impact crater clusters in high resolution HiRISE images. Lunar Planet. Sci. 39, #1221.
Ivanov, B.A., Melosh, H.J., McEwen, A.S., and the HiRISE team, 2009. Small impact crater clusters in high resolution HiRISE images – II. Lunar Planet. Sci. 40, #1410.
Ivanov, B.A., Melosh, H.J., McEwen, A.S., and the HiRISE team, 2010. New small impact craters in high resolution HiRISE images – III. Lunar Planet. Sci. 41, #2020.
Kadish, S.J., Head, J.W., Parsons, R.L., Marchant, D.R., 2008. The Ascraeus Mons fan-shaped deposit: Volcano–ice interactions and the climatic implications of cold-based tropical mountain glaciation. Icarus 197, 84–109.
Kennedy, M.R., Malin, M.C., 2009. 100 New impact crater sites found on Mars. AGU Fall Meeting, #P43D-1455.
Kneissel, T., van Gasselt, S., Neukum, G., 2011. Map-projection-independent crater size–frequency determination in GIS environments – New software tool for ArcGIS. Planet. Space Sci. 59, 1243–1254.
Kovach, R.L., Watkins, J.S., 1973. The velocity structure of the lunar crust. Moon 7, 63–75.
Lanagan, P.D., McEwen, A.S., Keszthelyi, L.P., Thordarson, T., 2001. Rootless cones on Mars indicating the presence of shallow equatorial ground ice in recent times. Geophys. Res. Lett. 28, 2365–2367.
Love, S.G., Brownlee, D.E., 1991. Heating and thermal transformation of micrometeoroids entering the Earth's atmosphere. Icarus 89, 26–43.
Malin, M.C., Edgett, K.S., 2000a. Evidence for recent groundwater seepage and surface runoff on Mars. Science 288, 2330–2335.
Malin, M.C., Edgett, K.S., 2000b. Sedimentary rocks of early Mars. Science 290, 1927–1937.
Malin, M.C., Edgett, K.S., 2001. Mars Global Surveyor Mars Orbiter Camera: Interplanetary cruise through primary mission. J. Geophys. Res. 106, 23429–23570.
Malin, M.C. et al., 1992. Mars orbiter camera. J. Geophys. Res. 97, 7699–7718.
Malin, M.C., Edgett, K.S., Posiolova, L., McColley, S., Noe Dobrea, E., 2006. Present impact cratering rate and the contemporary gully activity on Mars: Results of the Mars Global Surveyor extended mission. Science 314, 1573–1577.
Malin, M.C. et al., 2007. Context Camera investigation on board the Mars Reconnaissance Orbiter. J. Geophys. Res. 112, E05S04. http://dx.doi.org/10.1029/2006JE002808.
Mangold, N., 2003. Geomorphic analysis of lobate debris aprons on Mars at Mars Orbiter Camera scale: Evidence for ice sublimation initiated by fractures. J. Geophys. Res. 108, GDS 2-1. http://dx.doi.org/10.1029/2002JE001885.
Marchi, S., Mottola, S., Cremonese, G., Massironi, M., Martellato, E., 2009. A new chronology for the Moon and Mercury. Astron. J. 137, 4936–4948.
Marquez, A., Fernandez, C., Anguita, F., Farelo, A., Anguita, J., de la Casa, M.-A., 2004. New evidence for a volcanically, tectonically, and climatically active Mars. Icarus 172, 573–581.
McEwen, A.S., Bierhaus, E.B., 2006. The importance of secondary cratering to age constraints on planetary surfaces. Annu. Rev. Earth Planet. Sci. 34, 535–567.
McEwen, A.S., Preblich, B.S., Turtle, E.P., Artemieva, N.A., Golombek, M.P., Hurst, M., Kirk, R.L., Burr, D.M., Christensen, P.R., 2005. The rayed crater Zunil and interpretations of small impact craters on Mars. Icarus 176, 351–381. http://dx.doi.org/10.1016/j.icarus.2005.02.009.
McEwen, A.S. et al., 2007a. Mars Reconnaissance Orbiter's High Resolution Imaging Science Experiment (HiRISE). J. Geophys. Res. 112, E05S02. http://dx.doi.org/10.1029/2005JE002605.
McEwen, A.S., Grant, J.A., Tornabene, L.L., Byrne, S., Herkenhoff, K.E., 2007b. HiRISE observations of small impact craters on Mars. Lunar Planet. Sci. 38, #2009.
McEwen, A.S., Tornabene, L.L., and the HiRISE Team, 2007c. Modern Mars: HiRISE observations of small, recent impact craters on Mars. Lunar Planet. Sci. 7, #3086 (LPI Contribution No. 1353).
Melosh, H.J., 1989. Impact Cratering: A Geologic Process. Oxford Univ. Press, New York, 245 pp..
Michael, G.G., Neukum, G., 2010. Planetary surface dating from crater size–frequency distribution measurements: Partial resurfacing events and statistical age uncertainty. Earth Planet. Sci. Lett. 294, 223–229.
Moore, H.J., Boyce, J.M., Hahn, D.A., 1980. Small impact craters in the lunar regolith – Their morphologies, relative ages, and rates of formation. Moon Planet. 23, 231–252.
Neukum, G., Ivanov, B.A., 1994. Crater size distributions and impact probabilities on Earth from lunar, terrestrial-planet, and asteroid cratering data. In: Gehrels, T., Matthews, M.S., Schumann, A.M. (Eds.), Hazards Due to Comets and Asteroids. Univ. of Arizona, Tucson, pp. 359–416.
Neukum, G., Wise, D., 1976. Mars: A standard crater curve and possible new time scale. Science 194, 1381–1387.
Neukum, G., Ivanov, B.A., Hartmann, W.K., 2001. Cratering records in the inner Solar System in relation to the lunar reference system. Space Sci. Rev. 96, 55–86.
Osinski, G.R., Tornabene, L.L., Grieve, R.A.F., 2011. Impact ejecta emplacement on terrestrial planets. Earth Planet Sci. Lett. 310, 167–181.
Podolak, M., Pollack, J.B., Reynolds, R.T., 1988. Interactions of planetesimals with protoplanetary atmospheres. Icarus 73, 163–179.
Popova, O., Nemtchinov, I., Hartmann, W.K., 2003. Bolides in the present and past martian atmosphere and effects on cratering processes. Meteorit. Planet. Sci. 38, 905–925.
Popova, O., Hartmann, W.K., Nemtchinov, I., Richardson, D.C., Berman, D.C., 2007. Crater clusters on Mars: Shedding light on martian ejecta launch conditions. Icarus 190, 50–73.
Popova, O. et al., 2011. Very low strengths of interplanetary meteoroids and small asteroids. Meteorit. Planet. Sci. 46, 1525–1550.
Quantin, C., Mangold, N., Hartmann, W.K., Allemand, P., 2007. Possible long-term decline in impact rates 1. Martian geological data. Icarus 186, 1–10.
Reiss, D., van Gasselt, S., Neukum, G., Jaumann, R., 2004. Absolute dune ages and implications for the time of formation of gullies in Nirgal Vallis, Mars. J. Geophys. Res. 109, E06007. http://dx.doi.org/10.1029/2004JE002251.
Schon, S.C., Head, J.W., Fassett, C.I., 2009. Unique chronostratigraphic marker in depositional fan stratigraphy on Mars: Evidence for ca. 1.25 Ma gully activity and surficial meltwater origin. Geology 37, 207–210.
Scott, D.H., Dohm, J.M., Zimbelman, J.R., 1998. Geologic Map of Pavonis Mons Volcano, Mars. US Geol. Surv. Misc. Invest. Ser. Map I-2561.
Shean, D.E., Head, J.W., Kreslavsky, M., Neukum, G., and HRSC Co-I Team, 2006. When were glaciers present in Tharsis? Constraining age estimates for the Tharis Montes fan-shaped deposits. Lunar Planet. Sci. 37, #2092.
Smith, D.E. et al., 1999. The global topography of Mars and implications for surface evolution. Science 284, 1495–1503.
Stöffler, D., Ryder, G., 2001. Stratigraphy and isotope ages of lunar geologic units: Chronological standard for the inner Solar System. Space Sci. Rev. 96, 9–54.
Svetsov, V.V., Nemtchinov, I.V., Teterev, A.V., 1995. Disintegration of large meteoroids in Earth's atmosphere: Theoretical models. Icarus 116, 131–153.
Tornabene, L.L., Osinski, G.R., McEwen, A.S., Boyce, J.M., Bray, V.J., Caudill, C.M., Grant, J.A., Hamilton, C.W., Mattson, S., Mouginis-Mark, P.J., 2012. Widespread crater-related pitted materials on Mars: Further evidence for the role of target volatiles during the impact process. Icarus 220, 348–368.
Watkins, J.S., Kovach, R.L., 1973. Seismic investigation of the lunar regolith. Proc. Lunar Sci. Conf. 3, 2561–2574.
Weibull, W.A., 1951. A statistical distribution function of wide applicability. J. Appl. Mech. 10, 140–147.
Wilhelms, D.E., 1987. The geologic history of the Moon. U.S. Geol. Surv. Prof. Pap., 1348, 302pp.